PAPER

Check for updates

In situ crosslinkable poly(carbonate-ether-urethane) binders with 100% thermal decomposability at low temperatures for dry-processed high-capacity LiFePO₄ cathodes†

Bin Chen,[a] Zhe Zhang,[a] Sheng Huang,[b] Andrey B. Yaroslavtsev,[d] Min Xiao,[b] Shuanjin Wang,[b] Hui Guo, [ID][a] Dongmei Han*[a,b] and Yuezhong Meng [ID] *[a,b,c]

The commercially available polyvinylidene fluoride (PVDF) binder is commonly used as a battery binder for lithium iron phosphate batteries (LiFePO₄, LFP). Fluorine-containing PVDF not only causes environmental risks but also impedes Li⁺ transport due to its low ionic conductivity, limiting the performance of LFP electrodes. Traditional electrode fabrication processes rely on solvents, resulting in environmental pollution and high energy consumption. In this study, we selected commercial polycarbonate diol (PPCDL) and polyether polyol as binder monomers, utilizing hexamethylene diisocyanate trimers (HDI trimers) as crosslinking agents. Through an *in situ* thermal initiation method, we developed a cross-linked polyurethane (CPU) binder exhibiting excellent ionic conductivity. By integrating this binder with a solvent-free method, high-loading dry LFP electrodes were fabricated. The assembled LFP∥Li battery achieved an initial discharge capacity of 146 mAh g⁻¹ with a capacity retention of 97.5% over 100 cycles at 0.5C. Furthermore, the LFP∥Gr full cell exhibited a longer cycle life and higher discharge capacity under identical conditions. Notably, the CPU binder was decomposable and could be completely decomposed at 400 °C, thereby facilitating electrode recovery and reducing energy consumption. This innovative binder preparation strategy, coupled with the solvent-free electrode fabrication process, enhances the competitiveness of dry electrode commercialization by reducing energy consumption greatly and eliminating volatile organic compound (VOC) emissions.

Broader context

The fluorine-containing PVDF binder causes environmental pollution and restricts Li⁺ transport, while traditional solvent-based processes are energy-intensive. This study developed a thermally crosslinked polyurethane (CPU) binder using polycarbonate diol, polyether polyol, and HDI trimers, coupled with a solvent-free process to fabricate high-performance, high-loading LFP electrodes. (1) In the electrode recovery process, the battery using CPU as the binder can be 100% decomposed at low temperatures (400 °C or lower), which has great advantages over PVDF (600–800 °C, incomplete decomposition, producing toxic substances such as HF). The batteries assembled from the powder after four recycling cycles still have over 97% of the original capacity. (2) The CPU binder has a cross-linked structure that is resistant to electrolyte dissolution and also has a certain degree of solubility, which helps to build Li⁺ transport channels. Both the carbonates in the PPCDL segment and the ether bonds in the polyether polyol segment contribute to the excellent ionic conductivity, which reduces electrochemical impedance. (3) We are the first to work on combining *in situ* cross-linking with dry electrodes. This method significantly shortens the electrode preparation process while enabling the preparation of high loading electrodes (>20 mg cm⁻²).

[a]School of Chemical Engineering and Technology, Sun Yat-sen University, Zhuhai 519000, PR China. E-mail: chenb223@mail2.sysu.edu.cn, zhangzh569@mail2.sysu.edu.cn, guoh37@mail.sysu.edu.cn, handongm@mail.sysu.edu.cn, mengyz@mail.sysu.edu.cn
[b]The Key Laboratory of Low-Carbon Chemistry & Energy Conservation of Guangdong Province/State Key Laboratory of Optoelectronic Materials and Technologies, School of Materials Science and Engineering, Sun Yat-sen University, Guangzhou 510275, PR China.

E-mail: huangsh47@mail.sysu.edu.cn, stsxm@mail.sysu.edu.cn, wangshj@mail.sysu.edu.cn
[c]Institute of Chemistry, Henan Academy of Sciences, Zhengzhou 450000, PR China
[d]Ionics of Functional Materials Laboratory, Kurnakov Institute of General and Inorganic Chemistry, RAS, Leninsky Prospect, 31, Moscow, 119991, Russian Federation. E-mail: yaroslav@igic.ras.ru
†Electronic supplementary information (ESI) available. See DOI: https://doi.org/10.1039/d5eb00093a

1. Introduction

The lithium-ion battery (LIB) is a well-established energy storage technology and has been widely used in various fields, such as digital products, energy storage stations, and new energy vehicles. As technology advances, the performance requirements for LIBs continue to increase. Currently, these batteries are being developed to offer higher safety, better performance, and lower costs, making them a long-standing focus of research. Most studies focus primarily on electrolytes,[1–3] with less attention given to other components of the battery. However, the performance and sustainability of LIBs are also critically influenced by other components, such as binders, which have received insufficient attention despite their vital role in electrode integrity and recyclability.

Binders are essential materials in electrodes. With the emergence of new active materials, particularly the development of silicon electrodes, there has been increasing emphasis on the development and modification of binders.[4–7] In commercial electrodes, binders typically account for only 1–5% of the total mass, yet they play a crucial role in ensuring that other electrode materials adhere tightly to the current collector, thus maintaining the integrity and stability of the electrode structure during battery cycling.[8–10] Currently, polyvinylidene fluoride (PVDF) is the most commonly used binder for cathodes. Its molecular structure consists of long chains that interact with electrode materials and current collectors through physical forces, such as van der Waals forces, providing adhesive strength. Moreover, PVDF exhibits excellent dispersibility in organic solvents, allowing it to mix with electrode materials without the need for any surfactants or stabilizers. More importantly, PVDF possesses a very wide electrochemical window, demonstrating high electrochemical stability.[11]

However, PVDF faces three critical limitations: (1) poor ionic conductivity increasing electrode impedance;[12] (2) chemical inertness hindering functional modification;[13] and (3) thermal decomposition releasing toxic fluorinated by-products.[14] Although solvent recovery is possible, the use of organic solvents often results in environmental pollution, which has hinders its further adoption. High-temperature calcination is the most common method for electrode recycling, but PVDF requires elevated temperatures for complete decomposition, generating hydrogen fluoride and other harmful fluorinated compounds. These by-products pose environmental risks. Furthermore, during the traditional electrode preparation process, PVDF is mixed with organic solvents, such as N-methyl-2-pyrrolidone (NMP), to form a uniform slurry.[15] This slurry requires subsequent drying and solvent recovery, both of which are energy-intensive processes. The drying step alone accounts for 10–15% of the energy consumed in battery production, further raising concerns about energy efficiency and environmental impact.[16–18] Thus, the emergence of dry electrodes is a significant development. Dry electrodes eliminate the need for solvents, thereby removing the subsequent drying process and greatly reducing the production cost of batteries. Moreover, in the absence of the capillary effect during solvent drying, the binder in dry electrodes is often more evenly distributed.[19–21] This provides an ideal condition for preparing high-loading electrodes. Compared to traditional wet-process electrodes, dry electrodes typically exhibit higher energy density and lower electrochemical impedance, which are crucial for the fabrication of high-performance batteries.[22] This solvent-free approach necessitates binders with enhanced ionic conductivity and adhesion to compensate for the absence of solvent-induced material dispersion. In recent years, increasing research has focused on dry electrodes, investigating the manufacturing processes[23–26] and binders[27–29] used in their production, which has significantly accelerated the development of dry electrode technology. Many studies[30–34] have combined dry electrodes with solid-state electrolytes, achieving promising results.

To overcome the trade-off between binder functionality and environmental sustainability in dry electrodes, we have explored the use of various polycarbonate-based polymers as binders for LFP electrodes.[35–37] Furthermore, we also attempted to use polycarbonate-based polymers for NCM electrodes.[38] Here, we designed a novel cross-linked polyurethane (CPU) binder through *in situ* crosslinking of commercial polycarbonate diol (PPCDL, derived from industrial CO_2 waste[39]) and polyether polyol monomers, using hexamethylene diisocyanate trimers (HDI trimers) as the crosslinking agent. PPCDL provides dual functionality: its carbonate groups coordinate with Li^+ *via* lone-pair electrons to enhance ion transport, while its CO_2-derived backbone aligns with circular economy goals. The crosslinking process forms a three-dimensional network structure through chemical bond interactions between polyurethane molecular chains, significantly improving intermolecular forces and interfacial adhesion. Polyether polyol further contributes to Li^+ conductivity through its ether bonds. As illustrated in Fig. 1, this solvent-free fabrication enables scalable hot-pressing of high-loading LFP cathodes (~20 mg cm^{-2}), eliminating energy-intensive drying steps. Compared to PVDF-based electrodes (PVDF-LFP), the CPU-LFP cathodes exhibit higher peel strength due to the robust crosslinked architecture.

The synergistic effects of the CPU binder translate to a superior electrochemical performance. Lithium metal batteries with CPU-LFP cathodes achieve 97.5% capacity retention after 100 cycles at 0.5C, better than PVDF-LFP. They also exhibit enhanced rate capability and reduced interfacial impedance. Full cells pairing CPU-LFP cathodes with high-loading graphite (Gr) anodes (~10 mg cm^{-2}) show extended cycle life and higher discharge capacity. Notably, the CPU binder enables facile electrode powder recycling, with regenerated batteries retaining ~97% of their original capacity. This work highlights a cost-effective, sustainable strategy integrating CO_2 utilization, solvent-free processing, and high-performance binder design to advance lithium-ion battery manufacturing.

2. Results and discussion

In designing the segmental structure of the CPU, the ratio of polycarbonate to polyether segments was optimized to balance
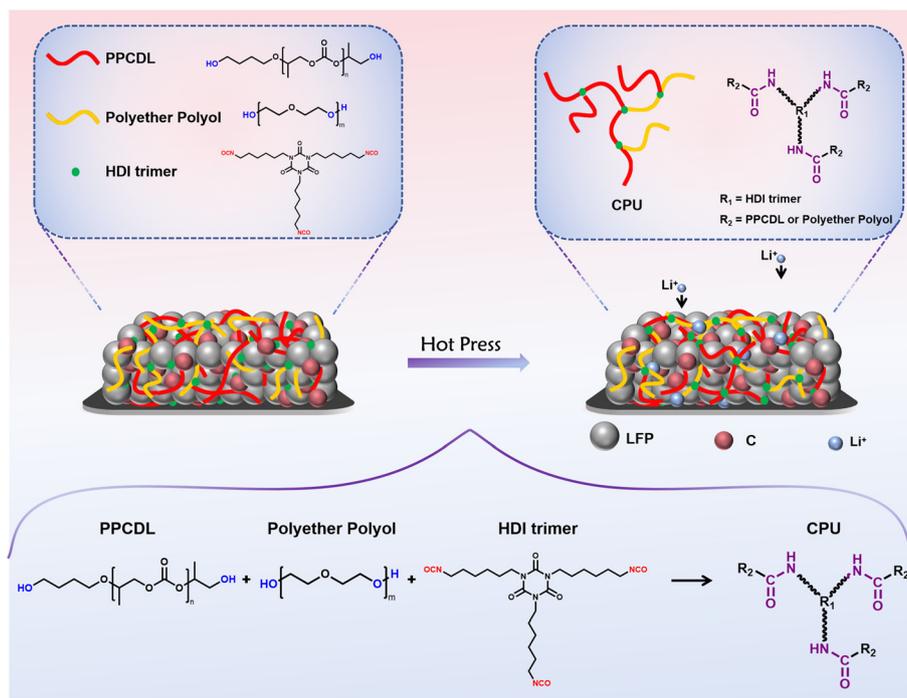
Fig. 1 Schematic diagram of the LFP electrode composition and synthesis scheme of the CPU binder.

the trade-off between mechanical robustness and ionic conductivity. Specifically, the polycarbonate segments, with their high-polarity carbonate groups, facilitate Li$^+$ migration through coordination interactions, while the flexible polyether segments enhance chain mobility to lower ion transport energy barriers. To select a more suitable mixing ratio, we evaluated it based on the curing effect and ionic conductivity (Table 1). After infiltration by the electrolyte, the lithium-ion (Li$^+$) conductivity of the CPU binder and PVDF binder films was evaluated at 30 °C to simulate their actual situation in the electrode.[40,41] The results show that CPU has excellent ion conductivity (molar ratio of PPCDL : polyether polyol = 7 : 3, 3.3×10^{-5} S cm^{-1}), significantly higher than that of PVDF (5.6×10^{-7} S cm^{-1}). This can be attributed to the abundant carbonate groups in PPCDL segments and ether bonds in the polyether polyol segments of the CPU polymer, which effectively promote the transport of Li$^+$. The outstanding ion conduction performance also helps reduce internal resistance and improve battery performance. In the subsequent tests, a binder with a molar ratio of PPCDL : polyether polyol = 7 : 3 was used.

Table 1 Ionic conductivity for the thermally crosslinked CPU and PVDF samples

	PPCDL : polyether polyol	–OH : –NCO	State	Temp. (°C)	σ (S cm^{-1})
CPU1	3 : 7	1 : 1	Solid–liquid	—	—
CPU2	5 : 5	1 : 1	Solid	30	1.9×10^{-5}
CPU3	7 : 3	1 : 1	Solid	30	3.3×10^{-5}
PVDF	—	—	Solid	30	5.6×10^{-7}

To further confirm the presence of the crosslinked structure in CPU, infrared spectroscopy was performed on the binder monomers, crosslinking agent, and cross-linked CPU (Fig. 2(a)). Multiple characteristic peaks appeared in the 4000–2000 cm^{-1} range. The peak at 2254.2 cm^{-1} in the HDI trimer curve corresponds to the characteristic absorption of –NCO. However, no significant peak is observed near this position in the CPU curve, indicating that there is no residual –NCO in the crosslinked CPU. Both curves exhibit two peaks around 2900 cm^{-1}, which correspond to the stretching vibrations of –CH$_3$ and –CH$_2$ groups. The peak at 3411.1 cm^{-1} in the polyether polyol curve and the peak at 3530.1 cm^{-1} in the PPCDL curve correspond to the characteristic absorption of –OH groups. Although a peak is also observed at 3350.5 cm^{-1} in the CPU curve, it is shifted slightly compared to the peaks in the polyether polyol and PPCDL curves. This shift is due to the presence of an N–H absorption peak near this position. Fig. 2(b) shows an enlarged spectrum in the 1800–500 cm^{-1} range. In the CPU curve, the peak at 1745.5 cm^{-1} corresponds to the C=O stretching vibration of the ester bond in the PPCDL segment. The corresponding peak position shifts to 1745.5 cm^{-1} on CPU, indicating the formation of hydrogen bonds. The peak at 1681.5 cm^{-1} is associated with the C=O stretching vibration in the carbamate bond of the HDI trimer segment. The peak at 1526.3 cm^{-1} corresponds to the N–H bending vibration in the urethane bond, indicating the successful synthesis of CPU.

After mixing the two binder monomers with the crosslinking agent in the specified ratio, the mixture was heated at 120 °C for 20 minutes (Fig. S2†). The resulting mixture exhibi-
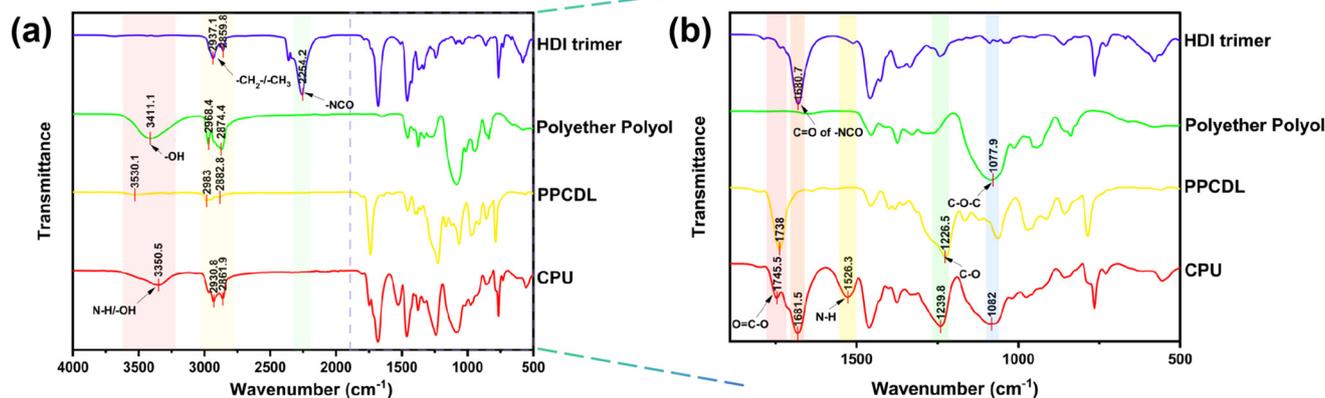
Fig. 2 (a and b) FTIR spectra for the binder monomers and CPU.

ted excellent flowability, with no significant solid formation observed, indicating that no detectable crosslinking reaction occurred during the high-speed stirring process. Subsequently, the two binder monomers were mixed with the crosslinking agent in the same ratio and heated at 170 °C for 20 minutes (Fig. S3†). The resulting mixture formed a translucent, off-white solid with no visible liquid phase, confirming that a significant crosslinking reaction occurred under these conditions.

To verify successful crosslinking between the binder monomers and the crosslinker under heating conditions, we performed gel permeation chromatography (GPC) on the soluble portion of the crosslinked CPU. Fig. S4† shows a marked shift in the elution peak of the soluble portion toward lower retention times, indicating the formation of higher molecular weight polymers, thereby validating the crosslinking reaction.

The contact angles between the electrolyte and the binder films were measured (Fig. S5†). The results revealed a smaller contact angle for the PVDF film compared to CPU, suggesting stronger electrolyte–PVDF affinity. However, the CPU film exhibited a contact angle of approximately 32°, still showing favorable electrolyte compatibility.

Fig. 3(a) shows the DSC curves of different binders and binder monomers. The results reveal that the CPU binder is an amorphous material with a very low glass transition temperature (T_g) of 6.8 °C, whereas PVDF exhibits a melting point (T_m) of 161.4 °C. During the charging and discharging process of the battery, the operating temperature (∼30 °C) exceeds the T_g of CPU, inducing a transition to a highly elastic state. This rubbery state enhances CPU chain mobility, which generates additional free volume and creates interconnected pathways for ion transport, thereby improving ionic diffusion rates within the polymer matrix. Meanwhile, the enhanced chain mobility weakens the interactions between the polymer and ions. This reduction in binding allows for greater ionic mobility, often leading to higher ionic conductivity in the polymer. Finally, when CPU is in the rubbery state, its increased flexibility and stronger intermolecular interactions significantly

enhance its adhesive strength. This ensures close contact between the cathode material, carbon materials, and current collectors, maintaining the integrity of the electrode structure during battery cycling, thereby improving battery performance. DSC tests on the binder monomers under identical conditions (Fig. S6†) demonstrate their excellent flowability at 120 °C, which facilitates homogeneous dispersion of the monomers within the electrode powder during high-speed mixing.

The uniformity of the binder monomer dispersion in the electrode powder after high-speed stirring was evaluated by thermogravimetric analysis (TGA) under a nitrogen atmosphere. As shown in Fig. S7,† PPCDL and polyether polyol begin decomposing at approximately 200 °C and are fully decomposed by 350 °C. As shown in Fig. 3(b), the CPU binder synthesized *via in situ* thermal initiation starts decomposing at 200 °C and is completely decomposed at 500 °C, whereas PVDF retains ∼33% residue at 600 °C. This demonstrates that CPU binders can be readily decomposed, enabling separation from other electrode materials and facilitating electrode recycling upon battery disposal. The thermogravimetric curve of the CPU binders exhibits three distinct stages, primarily attributed to incomplete monomer reactions during the *in situ* process. Residual unreacted monomers failed to undergo crosslinking, leading to this phenomenon. TGA was performed *via* random sampling with multiple tests. Fig. 3(c) confirms the uniform binder dispersion in the powder. After the binder monomers are mixed with the powder, the presence of active materials and carbon materials might hinder the cross-linking reaction between the monomers, thereby altering the time required for substantial crosslinking to occur. To investigate this, we employed Soxhlet extraction to measure the cross-linking degree of the binder monomers under hot pressing at 170 °C for different durations (Fig. 3(d)). The results revealed a low crosslinking degree (<20%) within the first 40 minutes. When the heating time was extended to 60 minutes, the crosslinking degree exceeded ∼90%. The remaining unreacted binder monomer content is minimal, and carbonate and ether polymers are also common components of lithium-ion battery
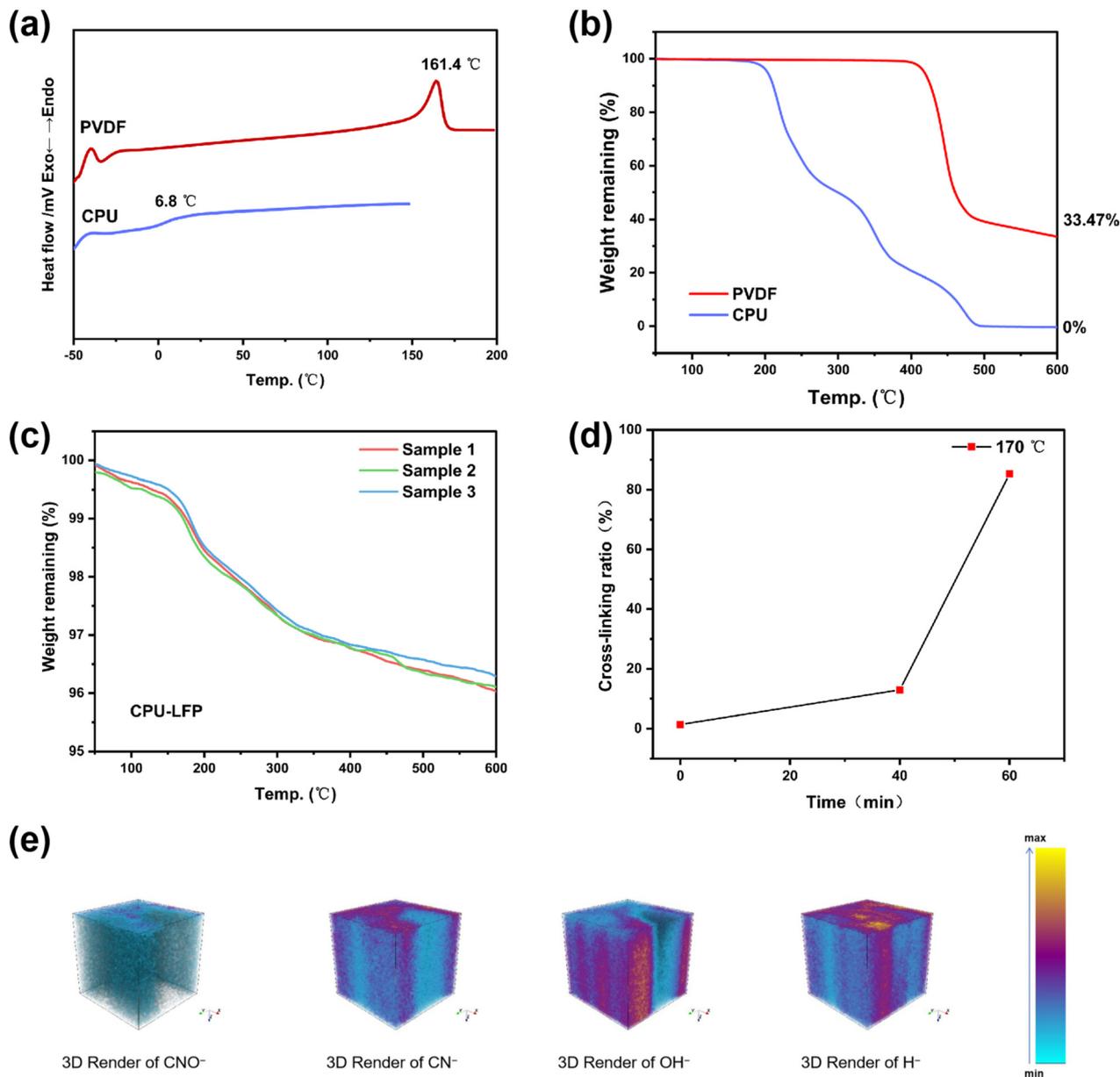
Fig. 3 (a) DSC spectra and (b) TGA spectra for PVDF and CPU, (c) TGA spectra for the electrode powder with the CPU binder, (d) cross-linking ratio of the monomers in the powder at 170 °C, and (e) 3D distribution of the CNO^-, CN^-, OH^- and H^- fragments in the CPU-LFP electrode acquired by TOF-SIMS.

electrolytes, so it is believed that they will not significantly affect battery operation. This explanation can also be confirmed by the subsequent battery performance results.

The cross-sectional image of the electrode further reveals tight interconnections between electrode materials with no apparent voids (Fig. S8†). The calculated compacted density reaches 1.6 mg cm^{-3}. Energy dispersive spectroscopy (EDS) mapping shows the uniform distribution of nitrogen, which further confirms the homogeneous dispersion of CPU within the electrode. The distribution of the polyurethane binder in the dry lithium iron phosphate electrode was further characterized by time-of-flight secondary ion mass spectrometry

(TOF-SIMS). A 3D depth profile (50 μm × 50 μm) revealed the distribution of CNO^-, CN^-, OH^-, and H^- across the electrode surface and bulk (Fig. 3(e)). While the CNO^- content was negligible, CN^- exhibited a uniform spatial distribution, except for one localized region showing significantly reduced intensity. This anomaly correlates with a carbon agglomerate, as evidenced by the complementary anion distribution maps (Fig. S9†).

The adhesive strength of the binder in the electrode is particularly important for maintaining structural integrity. Fig. 4(a) shows the load–indentation depth curves obtained from the nano-indentation test, which quantitatively reflects
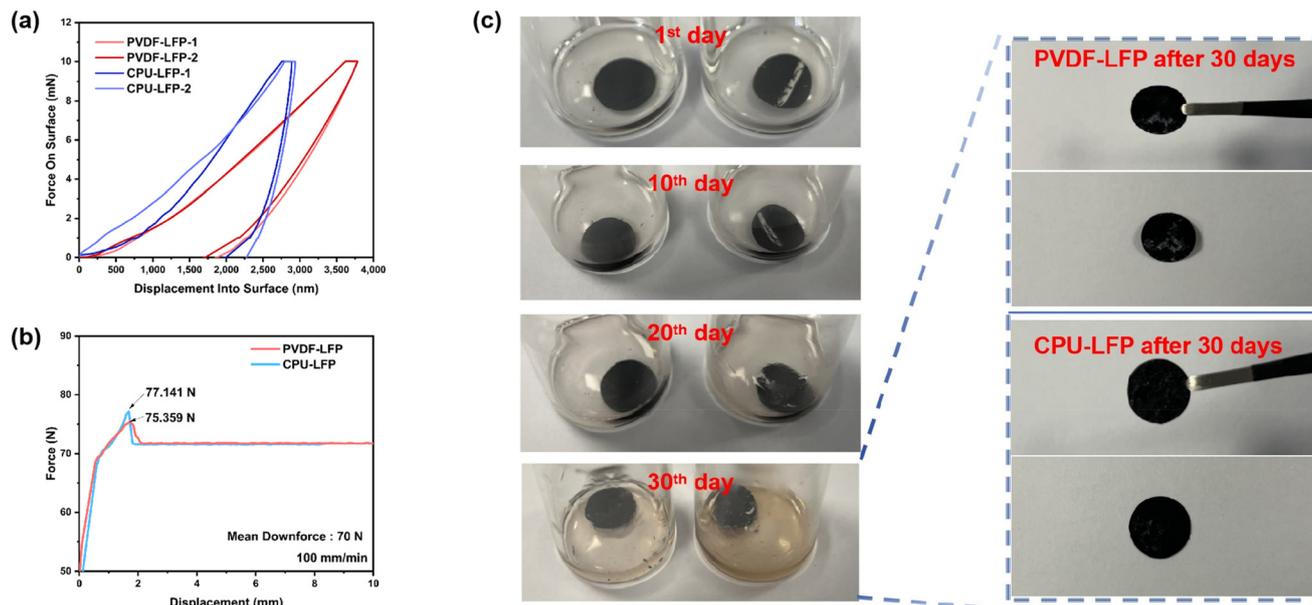
Fig. 4 (a) Load–indentation depth curves, (b) adhesion strengths of PVDF-LFP and CPU-LFP measured using the pull-off adhesion test, and (c) the test of the electrodes completely immersed in the electrolyte.

the adhesion performance of the binders. The results indicate that the CPU polymer binder exhibits significantly superior adhesion in dry electrodes compared to the PVDF binder. This enhancement originates from the highly crosslinked architecture of CPU, which promotes synergistic molecular interactions and restricted chain mobility. The three-dimensional crosslinked network improves mechanical robustness by increasing inter-chain connectivity and limiting segmental motion, thereby uniformly distributing mechanical stress across the electrode and optimizing adhesion. Furthermore, the covalent nature of crosslinking enables stronger polymer–substrate interfacial bonding, directly contributing to the observed adhesion improvement.

Fig. 4(b) presents the pull-off test results for different electrodes, with the test schematic illustrated in Fig. S1.† The results indicate that the electrodes using the CPU binder exhibit higher peel strength than those employing the PVDF binder, demonstrating CPU's superior adhesion properties. Fig. 4(c) shows the electrolyte immersion experiment, where electrodes were fully submerged for 30 days. Powder detachment was monitored every 10 days. The results indicate that both CPU-based electrodes and PVDF-based electrodes effectively prevented powder detachment, maintaining the structural integrity. This further demonstrates the superior adhesion properties of CPU and its resistance to dissolution in the electrolyte. Additionally, it confirms the reliability of the fabricated dry electrodes.

A series of electrochemical tests were conducted to evaluate the properties of the binder and the fabricated electrodes. The linear sweep voltammetry (LSV) curve (Fig. 5(a)) indicates that the CPU binder exhibits a wide electrochemical window (2.4–3.8 V *vs.* Li/Li$^+$) with stable chemical structure integrity

throughout this potential range. Fig. 5(b and c) present the electrochemical impedance spectroscopy (EIS) results of various electrodes, including Nyquist plots and equivalent circuit models after 10 and 100 cycles at 0.5C. The EIS curves reveal a high-frequency semi-circle, which indicates charge transfer resistance (R_{ct}), and a low-frequency line that reflects diffusion resistance. After 10 or 100 cycles, the CPU-based cathode exhibits the lowest R_{ct}, attributed to enhanced compatibility between CPU's ether/carbonate bonds and the carbonate-based electrolyte solvents, thereby optimizing the interfacial kinetics.

To evaluate the electrode performance, cyclic voltammetry (CV) was conducted at a scan rate of 0.1 mV s^{-1} (Fig. S10†). The CV curves for the CPU-based electrodes stabilized more rapidly over cycling, which was attributed to their lower interfacial impedance, promoting faster and more stable formation of the solid electrolyte interphase (SEI) film. Additionally, after stabilization (Fig. 5(d)), the CPU-based electrodes showed higher current responses and narrower voltage differences, indicating improved lithiation and delithiation kinetics. Fig. 5(e) presents the battery performance of half-cells composed of different cathodes and the lithium metal anode, cycled for 100 cycles at 0.5C. The cells were first activated for five cycles at 0.1C before cycling to 100 cycles at 0.5C. It is evident that the CPU-based cell exhibits significantly better stability and higher discharge specific capacity. The voltage-specific capacity graph (Fig. 5(g and h)) indicates that the CPU-based cell experiences lower polarization. These improvements could be attributed to the lower electrochemical impedance. Rate capability tests (Fig. 5(f)) show a stepwise capacity decline with increasing C-rates (0.1C → 2C → 1C). When the rate is reduced from 2C to 1C, the discharge capacity quickly
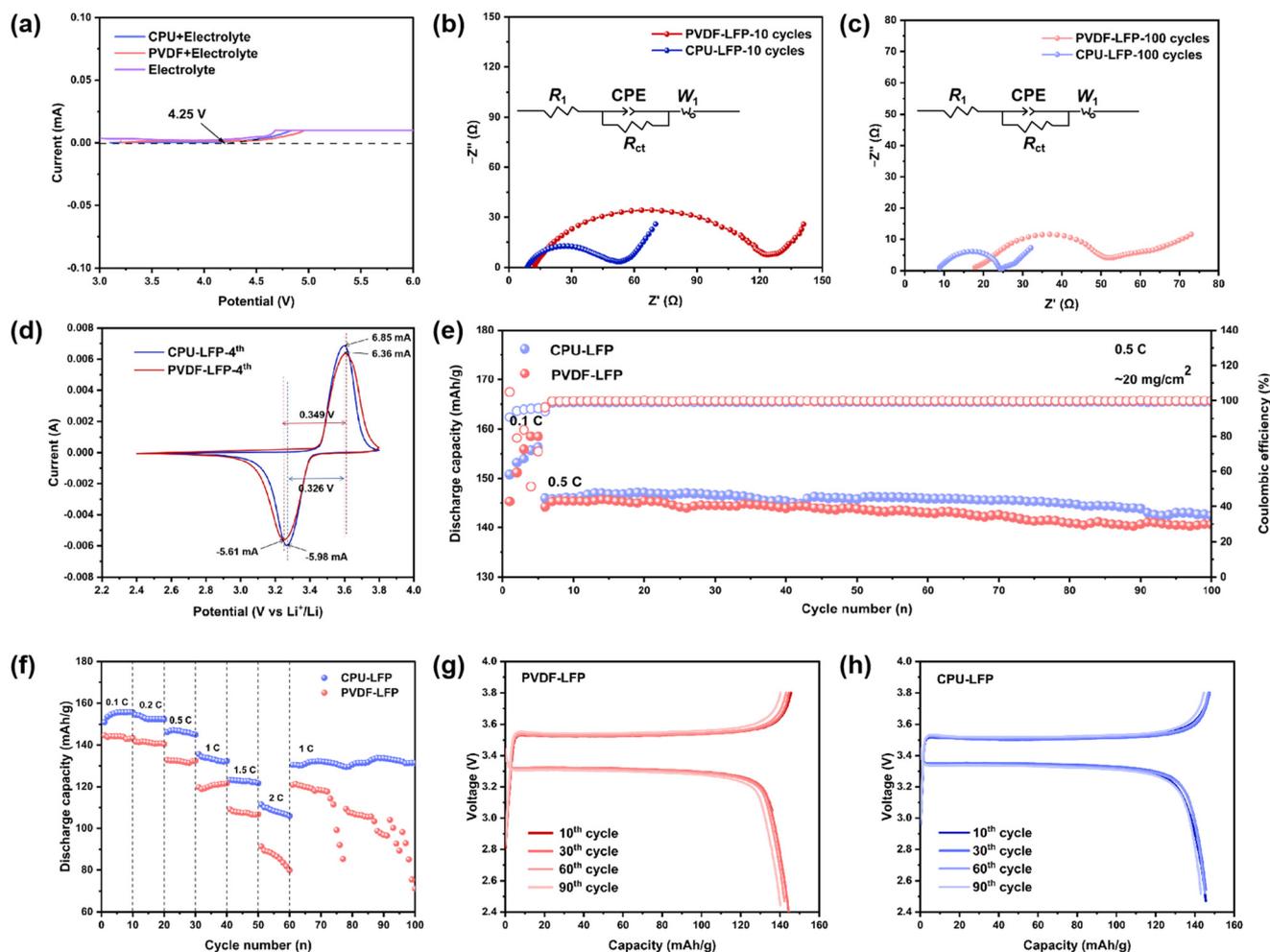
Fig. 5 (a) LSV curves of the CPU and PVDF binders, impedance comparisons of PVDF-LFP and CPU-LFP after (b) 10 and (c) 100 cycles at 0.5C, (d) CV curves of PVDF-LFP and CPU-LFP, (e) cycle performance and (f) rate performance of PVDF-LFP and CPU-LFP, and the 10th/30th/60th/90th galvanostatic charge/discharge curves of (g) PVDF-LFP and (h) CPU-LFP at 0.5C.

recovers to nearly its original value. This shows that the CPU-based cell exhibits a superior rate capacity performance, indicating that CPU effectively inhibits ohmic polarization, facilitating charging and discharging at varying rates. With continued cycling at 1C, the CPU-based cell shows excellent high rate cycling stability. In contrast, the PVDF-based cell shows rapid capacity degradation as well as instability.

In addition, we employed a galvanostatic intermittent titration technique (GITT) to assess the stability of the Li^+ diffusion coefficient (D_{Li^+}) in different electrodes (Fig. 6(a–c)). By calculating D_{Li^+} at each charge/discharge step, we generated curves illustrating the variation in D_{Li^+} (see the dotted lines below each image in Fig. 6(a and b)). Since the set voltage is reached before the completion of the last charge or discharge, there is a slight deviation in the calculated value of the final D_{Li^+}, which can be negligible. The results indicate that the CPU-based electrode exhibits a more stable D_{Li^+}. Fig. 6(d) presents the direct current internal resistance (DC-IR) test results. The internal resistance during the charging and discharging

processes was determined through linear regression analysis of the voltage *versus* current changes ($\Delta V–I$). The slopes of the $\Delta V–I$ curves for the CPU-based cells are relatively low, indicating that CPU binders, with their higher lithium-ion conductivity, are more effective than PVDF in reducing internal resistance. Consequently, CPU-based cells exhibit lower and more stable internal resistance compared to their PVDF counterparts.

The full-cell tests were conducted using graphite anodes (wet coating, loading 10 mg cm^{-2}). The assembled full cells show an N/P ratio of 1.05. Within the voltage range of 2.4–3.8 V (*vs.* Li/Li$^+$), five preconditioning cycles were performed at 0.1C, followed by a long-term cycling test at 0.5C. The results in Fig. 6(e) indicate that the CPU-based full cell achieved a higher initial capacity of 113.1 mAh g^{-1} with a capacity retention of 87.4% after 400 cycles, whereas the PVDF-based full cell exhibited a lower initial capacity (110.8 mAh g^{-1}) and capacity retention after 400 cycles (59.3%). Notably, the coulombic efficiency of the PVDF-based cell gradually declined after 400 cycles, while
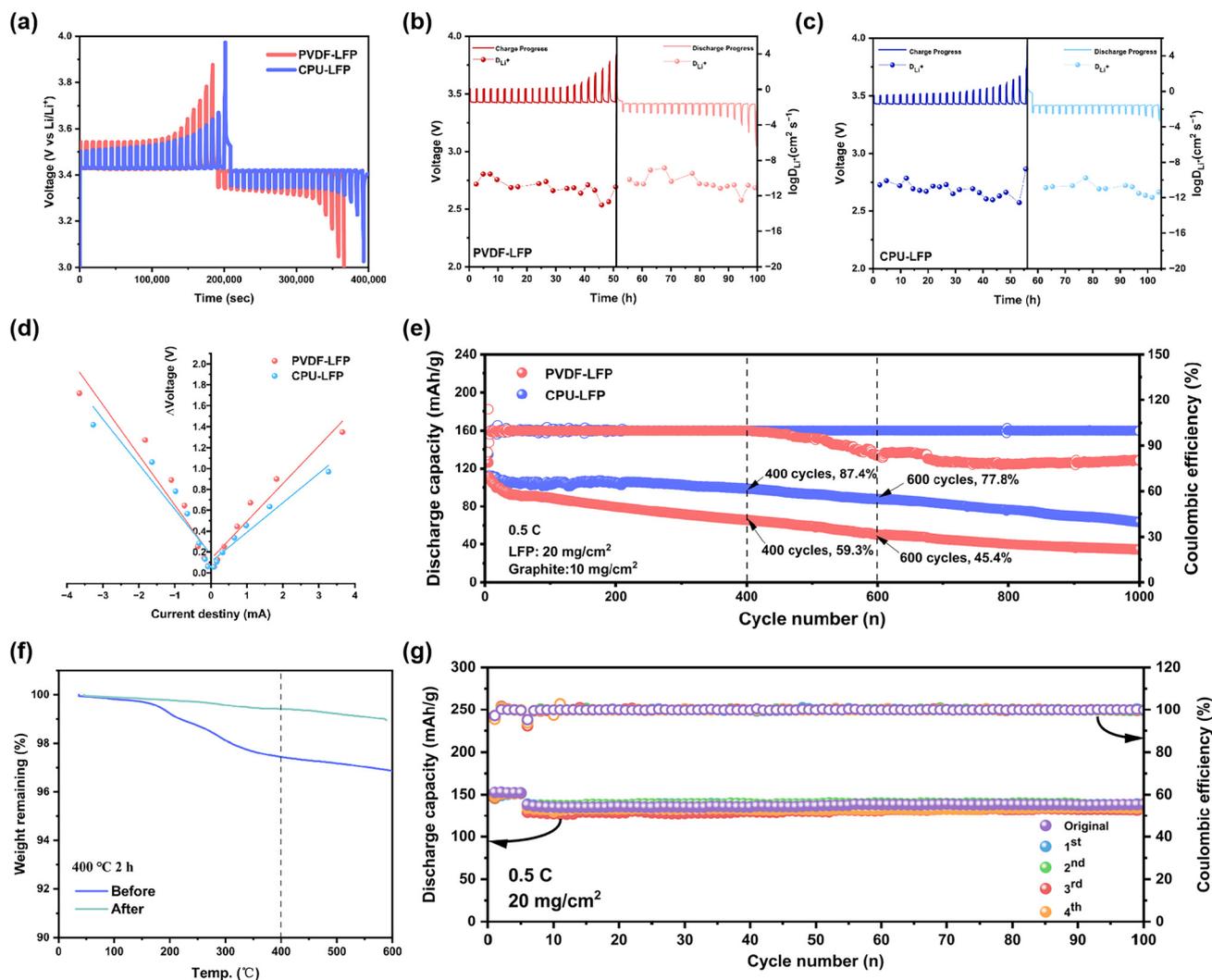
Fig. 6 (a) GITT profiles of the initial charge−discharge process for LFP||Li cells based on PVDF and CPU, voltage/D_{Li^+}−time curves of (b) PVDF-LFP and (c) CPU-LFP cells of the GITT test, (d) plots of the change in voltage *vs.* the current of different cells, and (e) cycling performance of the LFP||Gr full cell with an N/P ratio of 1.05 based on the PVDF and CPU binders at 0.5C. (f) TGA spectra of the CPU-based electrode powder before and after 400 °C roasting and (g) cycling test of the different batches of the electrode powder.

the CPU-based cell maintained a stable coulombic efficiency of >99.8% throughout the test (1000 cycles).

To demonstrate the advantages of the easy decomposition of the CPU binder, the electrode powder was subjected to high-temperature calcination (400 °C for 2 h) to decompose the binder, followed by the reintroduction of the binder for powder preparation. The TGA curve shows that the CPU binder is almost completely decomposed (as shown in Fig. 6(f)). As shown in Fig. 6(g), the half-cells assembled with CPU as the binder exhibit negligible capacity decay after 100 cycles at 0.5C. Remarkably, even after four cycles of recycling *via* calcination of the CPU binder, the half-cell retains a capacity retention rate of nearly 100% after 100 cycles at 0.5C. In previous works,[42,43] we confirmed that the decomposition products of PPC-based polymers are environmentally friendly. Additionally, studies have shown that thermal decomposition of polyurethane under an

inert atmosphere does not produce nitrogen oxides, resulting in a minimal environmental impact.[44]

Fig. 7(a and b) show the surface morphology of different electrodes before cycling and after 100 cycles at 0.5C. Before cycling, both electrodes exhibit tightly adhered active materials without any cracks. After 100 cycles, the PVDF-based electrode displays significant cracks, while the CPU-based electrode shows no noticeable cracks at a scale of 200 μm. Only when magnified to 50 μm can some minor cracks be observed. This difference arises because PVDF, being a linear structure, has a higher tendency to swell. Upon absorbing the electrolyte, PVDF undergoes substantial volume changes, disrupting the electrode structure. In contrast, although the CPU binder also shows affinity for the electrolyte, its lower swelling tendency and crosslinked structure provide greater toughness to withstand volume changes in the active materials, ultimately maintaining the integrity of the elec-
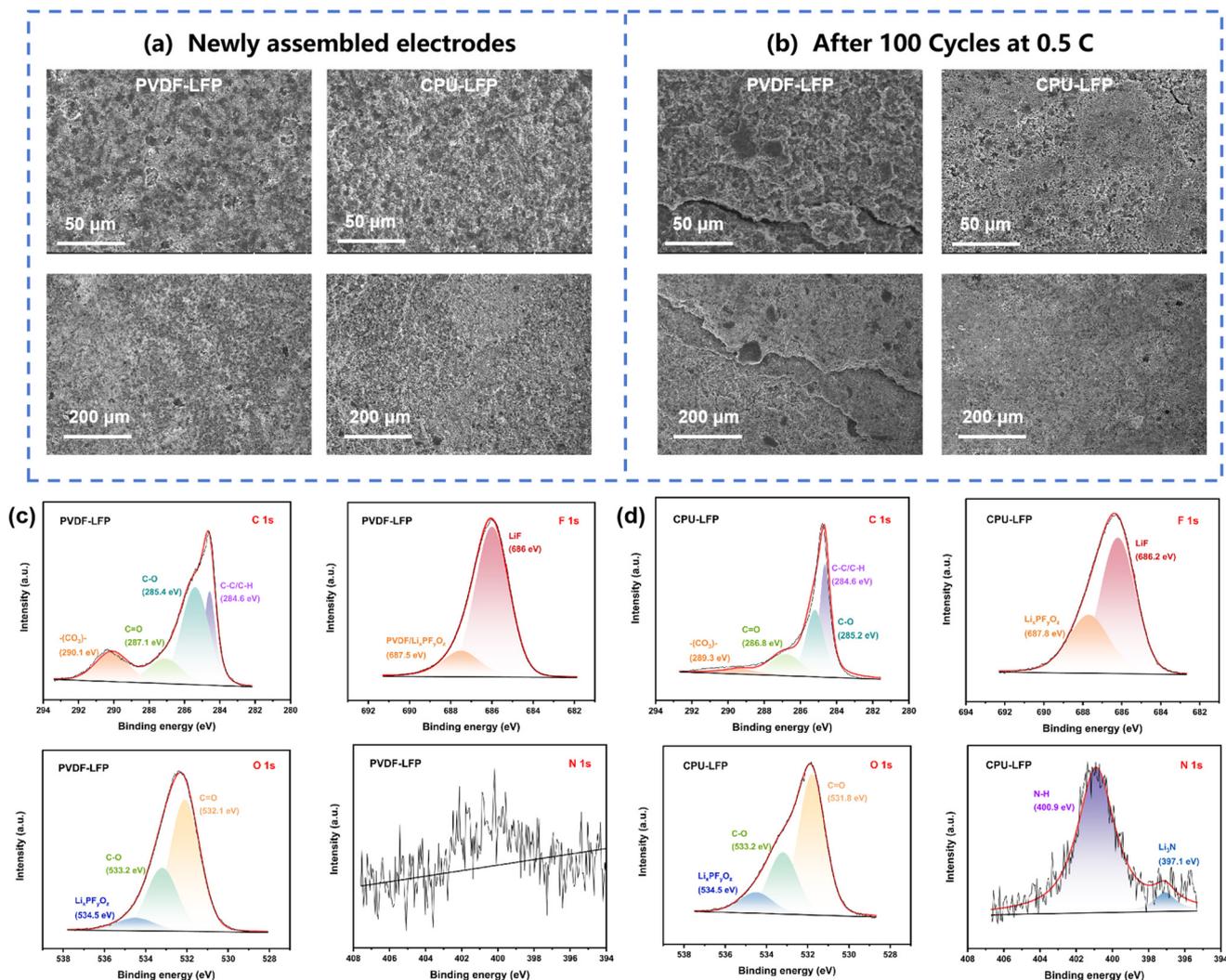
Fig. 7 SEM images of (a) PVDF–LFP and (b) CPU–LFP before and after 100 cycles at 0.5C, and the C 1s, F 1s, O 1s and N 1s XPS spectra of (c) PVDF–LFP and (d) CPU–LFP after 10 cycles at 0.1C.

trode structure. To investigate the role of CPU in cathode electrolyte interphase (CEI) film formation during the cycling process, XPS analysis was conducted on cycled cathodes (10 cycles at 0.1C; Fig. 7(c and d)). The results show that the CEI film compositions on both electrodes are similar, with no significant differences in the C 1s, F 1s, and O 1s spectra. However, in the N 1s spectrum, the CPU–LFP electrode displays distinct characteristic peaks at ~400.9 eV (N–H) and ~397.1 eV (Li_3N). In contrast, the N 1s spectrum of the PVDF–LFP electrode shows much higher noise, with no clear characteristic peaks. A weak peak is observed, which can be attributed to the incorporation of nitrogen atoms in the conductive carbon.

3. Conclusions

In conclusion, the use of *in situ* thermally induced crosslinking to prepare CPU as a binder for dry LFP electrodes

offers several advantages. First, the binder monomers (PPCDL and polyether polyol) are already industrially available, ensuring cost-effectiveness and scalability. Notably, PPCDL is derived from carbon dioxide, which not only enhances sustainability but also creates value-added use of greenhouse gases. Second, the CPU binder can be completely decomposed at 400 °C, facilitating electrode recycling without environmental hazards. The batteries assembled from powder after four recycling cycles still have over 97% of the original capacity. Third, with a low glass transition temperature, the CPU binder maintains elasticity during battery operation, ensuring excellent adhesion. The cross-linked structure also enhances the binder's ability to withstand volume expansion of the active electrode material during cycling. Additionally, both the carbonates in the PPCDL segment and the ether bonds in the polyether polyol segment contribute to the excellent ionic conductivity, which reduces electrochemical impedance. The dry LFP electrodes using this CPU binder show significantly lower

electrochemical impedance (EIS: ~50% lower than PVDF-LFP) and exhibit higher and more stable discharge capacities at 0.5C with long cycling stability (97.5% capacity retention after 100 cycles). As a result, the assembled LFP‖Gr full batteries show improved initial coulombic efficiency (88.04% *vs.* 83.56%), cycle life (87.4% *vs.* 59.3% capacity retention after 400 cycles) and discharge capacity.

This study innovatively combines *in situ* thermally induced crosslinking with solvent-free technology, providing new insights into the development of dry electrodes and binders. In the future, battery binders will likely evolve toward lower cost and more environmentally friendly options. Furthermore, binder design should focus not only on adhesion but also on addressing specific challenges of target electrodes, promoting the development of multifunctional binders. Ideally, these binders should be adaptable to a wide range of electrode types, enhancing their applicability in various battery technologies.

Conflicts of interest

The authors declare no competing financial interest.

Data availability

The data supporting this article have been included as part of the ESI.†

Acknowledgements

References

1 G. Su, Z. Zhang, M. Xiao, S. Wang, S. Huang, H. Guo, D. Han and Y. Meng, *Chem. Eng. J.*, 2024, **500**, 157050.

2 T. Wang, Y. Zhang, X. Huang, P. Su, M. Xiao, S. Wang, S. Huang, D. Han and Y. Meng, *SusMat*, 2024, **4**, e219.

3 Z. Zhang, Y. Ren, J. Liang, M. Xiao, S. Wang, S. Huang, D. Han and Y. Meng, *Energy Storage Mater.*, 2024, **71**, 103667.

4 T. Kwon, J. W. Choi and A. Coskun, *Chem. Soc. Rev.*, 2018, **47**, 2145.

5 L. Deng, Y. Zheng, X. Zheng, T. Or, Q. Ma, L. Qian, Y. Deng, A. Yu, J. Li and Z. Chen, *Adv. Energy Mater.*, 2022, **12**, 2200850.

6 F. B. Ajdari, F. Abbasi, A. M. Aghdam, F. G. C. Khaneh, A. G. Arjenaki, V. Farzaneh, A. Abbasi and S. Ramakrishna, *Mater. Sci. Eng., R*, 2024, **160**, 100830.

7 B. Chen, Z. Zhang, M. Xiao, S. Wang, S. Huang, D. Han and Y. Meng, *ChemElectroChem*, 2024, **11**, e202300651.

8 M. Lv, R. Zhao, Z. Hu, J. Yang, X. Han, Y. Wang, C. Wu and Y. Bai, *Energy Environ. Sci.*, 2024, **17**, 4871.

9 L. Zhang, X. Wu, W. Qian, K. Pan, X. Zhang, L. Li, M. Jia and S. Zhang, *Electrochem. Energy Rev.*, 2023, **6**, 36.

10 F. Zou and A. Manthiram, *Adv. Energy Mater.*, 2020, **10**, 2002508.

11 N. Lingappan, L. Kong and M. Pecht, *Renewable Sustainable Energy Rev.*, 2021, **147**, 111227.

12 Y. Ma, J. Ma and G. Cui, *Energy Storage Mater.*, 2019, **20**, 146.

13 H. Chen, M. Ling, L. Hencz, H. Y. Ling, G. Li, Z. Lin, G. Liu and S. Zhang, *Chem. Rev.*, 2018, **118**, 8936.

14 W. Dou, M. Zheng, W. Zhang, T. Liu, F. Wang, G. Wan, Y. Liu and X. Tao, *Adv. Funct. Mater.*, 2023, **33**, 2305161.

15 C. Chen, V. R. Tatagari, H. Lin and L. Shaw, *J. Energy Chem.*, 2023, **78**, 240.

16 N. Kim, J. Kim, H. Koo, J. Oh, J. Pang, K. Kang, S. Chae, J. Lim, K. W. Nam and S. Lee, *ACS Energy Lett.*, 2024, **9**, 5688.

17 Y. Lu, C. Zhao, H. Yuan, J. Hu, J. Huang and Q. Zhang, *Matter*, 2022, **5**, 876.

18 L. Jing, Y. Ji, L. Feng, X. Fu, X. He, Y. He, Z. Zhu, X. Sun, Z. Liu, M. Yang, W. Yang and Y. Wang, *Energy Storage Mater.*, 2022, **45**, 828.

19 J. Kim, K. Park, M. Kim, H. Lee, J. Choi, H. B. Park, H. Kim, J. Jang, Y. Kim, T. Song and U. Paik, *Adv. Energy Mater.*, 2024, **14**, 2303455.

20 N. Kumano, Y. Yamaguchi, Y. Akimoto, A. Ohshima, H. Nakamura and M. Yamamura, *J. Power Sources*, 2024, **591**, 233883.

21 C. Bak, K. Kim, H. Lee, S. Byun, M. Lim, H. An, Y. Roh, J. Lim, C. B. Dzakpasu, D. Kim, J. Lee, H. Lee, H. Lee and Y. M. Lee, *Chem. Eng. J.*, 2024, **483**, 148913.

22 N. Verdier, G. Foran, D. Lepage, A. Prebe, D. Ayme-Perrot and M. Dolle, *Polymers*, 2021, **13**, 323.

23 R. Tao, B. Steinhoff, X. Sun, K. Sardo, B. Skelly, H. M. M. C. Sawicki III, G. Polizos, X. Lyu, Z. Du, J. Yang, K. Hong and J. Li, *Chem. Eng. J.*, 2023, **471**, 144300.

24 D. Lee, Y. Shim, Y. Kim, G. Kwon, S. H. Choi, K. Kim and D. Yoo, *Nat. Commun.*, 2024, **15**, 4763.

25 K. Kwon, J. Kim, S. Han, J. Lee, H. Lee, J. Kwon, J. Lee, J. Seo, P. J. Kim, T. Song and J. Choi, *Small Sci.*, 2024, **4**, 2300302.

26 Z. Wei, D. Kong, L. Quan, J. He, J. Liu, Z. Tang, S. Chen, Q. Cai, R. Zhang, H. Liu, K. Xu, L. Xing and W. Li, *Joule*, 2024, **8**, 1350.

27 R. He, W. Zhong, C. Cai, S. Li, S. Cheng and J. Xie, *Adv. Energy Mater.*, 2024, **14**, 2402109.

28 J. Cha, S. Kim, U. T. Nakate and D. Kim, *J. Power Sources*, 2024, **613**, 234914.

29 L. Yuan, H. Liu and X. Jiang, *J. Energy Storage*, 2024, **90**, 111912.

30 J. Hu, H. Yuan, S. Yang, Y. Lu, S. Sun, J. Liu, Y. Liao, S. Li, C. Zhao and J. Huang, *J. Energy Chem.*, 2022, **71**, 612.

31 Y. Zhang, B. Gou, Y. Li, Y. Liao, J. Lu, L. Wu, W. Zhang, H. Xu and Y. Huang, *Chem. Eng. J.*, 2024, **498**, 155544.

32 D. Lee and A. Manthiram, *J. Mater. Chem. A*, 2024, **12**, 3323.

33 H. Kim, J. Y. Jung, K. Kim, C. Hwang, J. Yu, M. Park and W. Cho, *Adv. Energy Mater.*, 2024, **14**, 2303965.

34 S. Hong, Y. Lee, U. Kim, C. Bak, Y. M. Lee, W. Cho, H. J. Hah, Y. Sun and D. Kim, *ACS Energy Lett.*, 2022, **7**, 1092.

35 G. Xi, Z. Zhang, L. Zhong, S. Wang, M. Xiao, D. Han, S. Huang and Y. Meng, *Chem. Eng. J.*, 2024, **485**, 149983.

36 B. Chen, Z. Zhang, C. Wu, S. Huang, M. Xiao, S. Wang, H. Guo, D. Han and Y. Meng, *Materials*, 2024, **17**, 3153.

37 T. Zhao, S. Yang, S. Wang, D. Han, S. Huang, H. Guo, M. Xiao and Y. Meng, *Chem. Eng. J.*, 2025, **509**, 161097.

38 Z. Zhang, J. Ma, M. Xiao, S. Wang, S. Huang, H. Guo, D. Han and Y. Meng, *Materials*, 2024, **17**, 12.

39 X. Huang, K. Alferov, T. Zhao, J. Yin, S. Wang, D. Han, S. Huang, Z. Huang, M. Xiao and Y. Meng, *J. CO2 Util.*, 2023, **75**, 102571.

40 Z. Li, G. Wu, Y. Yang, Z. Wan, X. Zeng, L. Yan, S. Wu, M. Ling, C. Liang, K. N. Hui and Z. Lin, *Adv. Energy Mater.*, 2022, **12**, 2201197.

41 Z. Zhang, D. Han, M. Xiao, S. Wang, Y. Feng, S. Huang and Y. Meng, *Ionics*, 2023, **29**, 3895.

42 X. H. Li, Y. Z. Meng, Q. Zhu and S. C. Tjong, *Polym. Degrad. Stab.*, 2003, **81**, 157.

43 X. L. Lu, Q. Zhu and Y. Z. Meng, *Polym. Degrad. Stab.*, 2005, **89**, 282.

44 J. Oenema, H. Liu, N. D. Coensel, A. Eschenbacher, R. Van de Vijver, J. Weng, L. Li, C. Wang and K. M. Van Geem, *J. Anal. Appl. Pyrolysis*, 2022, **168**, 105723.